Electromagnetic scattering by curved surfaces and calculation of radiation force: Lattice Boltzmann simulations

Mohd. Meraj Khan ; Sumesh P. Thampi ; Anubhab Roy ✉

Check for updates

View Online   Export Citation

Electromagnetic scattering by curved surfaces and calculation of radiation force: Lattice Boltzmann simulations

View Online   Export Citation   CrossMark

Mohd. Meraj Khan,[1] [ID] Sumesh P. Thampi,[2] [ID] and Anubhab Roy[1,a) [ID]

AFFILIATIONS

[1]Department of Applied Mechanics and Biomedical Engineering, Indian Institute of Technology Madras, Chennai, India
[2]Department of Chemical Engineering, Indian Institute of Technology Madras, Chennai, India

[a)]Author to whom correspondence should be addressed: anubhab@iitm.ac.in. **URL:** https://home.iitm.ac.in/anubhab/

ABSTRACT

This study aims to investigate the effectiveness of the lattice Boltzmann method (LBM) in studying the scattering of electromagnetic waves by curved and complex surfaces. The computation of Maxwell's equations is done by solving for a pair of distribution functions, which evolve based on a two-step process of collision and streaming. LBM bypasses the need for expansion via vector spherical harmonics and thus is amenable to scatterers with complex geometries. We have employed LBM to compute the scattering width and radiation force for perfect electrically conducting and dielectric cylinders of circular and elliptical cross sections. Both smooth and corrugated surfaces are studied, and the results are compared against known analytical and numerical solutions from other methods. To ensure the broad applicability of the method, we have explored a wide range of parameter space—the dielectric constant and particle size to the wavelength ratio spanning Rayleigh, Mie, and geometrical optics regimes. Our simulations have successfully reproduced well-known analytical and numerical solutions, confirming the accuracy and reliability of the LBM for scattering calculations by complex-shaped objects.

I. INTRODUCTION

Scattering of electromagnetic (EM) waves is a fundamental phenomenon in physics and refers to the re-radiation of the incident wave due to interactions with a particle or object.[1] For example, the blue color of the sky or the red color of the sunset is due to the scattering of EM waves in the visible range of the spectrum.[2–4] Materials are composed of electric charges, i.e., electrons and protons. When an EM wave illuminates a material, the charges are set into oscillatory motion by the electric field of the incident wave. These oscillatory motions of the charges radiate EM waves in all directions called scattered radiation.[5] Scattering of the EM wave has applications in several fields, such as remote sensing, weather monitoring, radar-based rainfall rate estimation, medical science, and material science, to name a few.[6–10]

The scattering of an EM wave by an object results in the transfer of momentum from the EM field to the scattering object. The resulting force exerted by the wave on the object is called radiation force.[11] In laser physics, radiation force is utilized in a variety of applications; for example, in optical trapping and manipulation, focused laser beams trap and move microscopic particles.[12] Such techniques also have applications in biophysics, nanotechnology, material science, and in nano-robotics.[13,14] To compute the radiation force, detailed information about the scattering fields, namely, the incident and the scattered electric and magnetic fields at the surface of the scatterer[11] are required.

Scattering by cylindrical geometries is commonly encountered, for example, in the design of various devices, including antennas[15] and optical fibers.[16] Many natural structures, such as bacteria[17] and ice crystals,[18,19] can be effectively modeled as cylinders. Therefore, the scattering of EM waves by the cylindrical forms is a significant topic across multiple fields.

Extensive research has been conducted on EM wave scattering, with foundational work dating back nearly a century. Lord Rayleigh derived the exact solution for scattering by a circular dielectric cylinder under normal incidence,[20] followed by Wait, who addressed

oblique incidence for the same geometry.[21] Subsequent studies have expanded on scattering from circular cylinders[2,4,19] and other geometries such as hexagonal cylinders.[22,23]

The study of radiation forces on both circular and non-circular cylinders has garnered significant attention in recent research. De Zutter[24] analytically calculated the radiation force and torque on a rotating circular conducting cylinder. Xiao and Chan[25] employed the boundary element method to assess the radiation force on conducting and dielectric cylinders of arbitrary shapes. The radiation force on elliptical cylinders using diffraction theory was calculated by Rockstuhl and Herzig.[26] Additionally, Mitri[27–30] utilized both analytical and semi-analytical methods to compute the radiation forces and torques on various geometries, including circular, corrugated circular, elliptical, and corrugated elliptical cylinders. Further studies with multi-particles, for example, the radiation forces between a pair of cylinders have also been calculated.[31,32] These studies underscore the significance of determining radiation forces in applications such as optical manipulation and trapping.

Though different applications, the physics of scattering of radio waves by artificial satellites, microwave scattering from raindrops, and light scattering by aerosols,[4] are all similar, scattering phenomena depend on the ratio of the particle size to wavelength.[33] Based on a/λ, the ratio of the size of the scatterer (a) to the wavelength (λ), scattering phenomena can be divided into three regimes: (i) Rayleigh ($a/\lambda \ll 1$), (ii) Mie ($a/\lambda \sim 1$), and (iii) geometrical optics (GO) ($a/\lambda \gg 1$) regimes.[34] The blue color of the sky, the white color of the cloud, and the rainbow in the sky are examples of the scattering in the Rayleigh, Mie, and geometrical optics regimes, respectively.[2,5,34] Approximate analytical solutions are available to describe the scattering process in Rayleigh and geometrical optics regimes. In the Mie regime, scattering phenomena from the spheres and infinite circular cylinders of arbitrary radii made of homogeneous materials[2,34] can be solved exactly, coined with the term Mie theory. Although analytical and approximate analytical methods can handle electrically large objects (the object size much larger than the wavelength of the incident wave), the applicability of such methods is limited to only simple geometries. On the other hand, numerical methods can handle complex-shaped objects.[1]

Several numerical methods have been proposed in the literature to solve scattering problems:[35] the most common methods are T-matrix, separation of variables method (SVM), and finite-difference time-domain method (FDTD).[36] Numerical methods that are particularly useful to determine the scattered field from an arbitrarily shaped scatterer are the FDTD, finite element method (FEM), and discrete dipole approximation method (DDA).[35,36] FDTD is a flexible, fast, and easy method to implement, but it is only conditionally stable depending on the space discretization and time steps.[37] FEM is suitable for arbitrary-shaped and inhomogeneous scatterers, but the method's accuracy strongly depends, again, on spatial discretization.[38] DDA can handle objects of arbitrary shapes, but its numerical accuracy is low.[35] Also, FDTD and DDA are unsuitable for geometrical optics regime simulations as the computation time is very high.[36] Therefore, it is desirable to develop a stable numerical method to solve scattering problems by complex geometries without resorting to large computational times. This work proposes the lattice Boltzmann method (LBM) as an alternate numerical method to solve scattering problems.

LBM was originally developed as an efficient and stable alternative to conventional numerical methods for fluid dynamics simulations. LBM has been shown to be suitable for simulating flow through complicated geometries, such as flow through porous media, as this method does not need to trace the interfaces between different phases.[39] Due to the simplicity of the lattice Boltzmann equation, LBM is naturally adapted to parallel computing.[40] Other than fluid dynamics, LBM has also found applications in diverse simulating phenomena, including multi-component fluid flows,[41] heat transfer,[42] acoustics,[43] magnetohydrodynamics,[44] and electrodynamics.[45]

For the electrodynamics calculations, Mendoza and Muñoz[45] first presented an LBM implementation for EM wave propagation in homogeneous media, an implementation that was found to be faster than FDTD. They also mentioned that the numerical instability of LBM in inhomogeneous media could be avoided by smoothly transitioning between the two material properties. Hanasoge and co-authors[46] presented a lattice Boltzmann formulation for wave propagation in heterogeneous media, but their method also shows instability at a sharp interface between two different media. Liu and Yan[47] presented a different approach of LBM and used two equilibrium distribution functions for electric and magnetic fields. Their method showed improved accuracy for EM wave propagation. Hauser and Verhey[48] used the LBM given by Liu and Yan[47] and further improved the equilibrium distribution function. The method was found to be stable even at locations of a sharp transition in material properties, such as the interface between two media. In a separate study, Hauser and Verhey[49] conducted a comparison between LBM and FDTD. They discovered that LBM demands three times more memory and six times longer computation time than FDTD, given identical grid resolutions. However, to achieve the same level of error, LBM necessitates only one-third of the grid points required by FDTD. Consequently, LBM would consume nine times less memory and 18 times less computation time for equivalent accuracy.

Since LBM is a relatively new numerical method for electrodynamics computations, it is essential to verify its applicability for scattering problems by comparing it with available analytical solutions. Additionally, it is important to evaluate the performance of the LBM under various scattering regimes: Rayleigh, Mie, and geometrical optics, as they correspond to different length scales (scatterer's size compared to the wavelength). Other important aspects currently absent in the literature are the validation of LBM as a method to study scattering by complex objects of dielectric and conducting materials and the study of the behavior of LBM in materials with different dielectric materials. We undertake the tasks mentioned above in this paper and illustrate the validity of LBM in solving scattering problems by complex-shaped objects.

In Sec. II, we define the problem of scattering of electromagnetic waves. In Sec. III, we discuss the implementation of LBM, including the details of the computation domain and the initial and boundary conditions. Additionally, we explain the methodologies employed to calculate the scattering widths and radiation forces. The outcomes of the simulations are presented in Sec. IV. This section compares the numerical and analytical results for the scattering widths and radiation forces associated with perfect electrically conducting (PEC) and dielectric cylinders. The method is
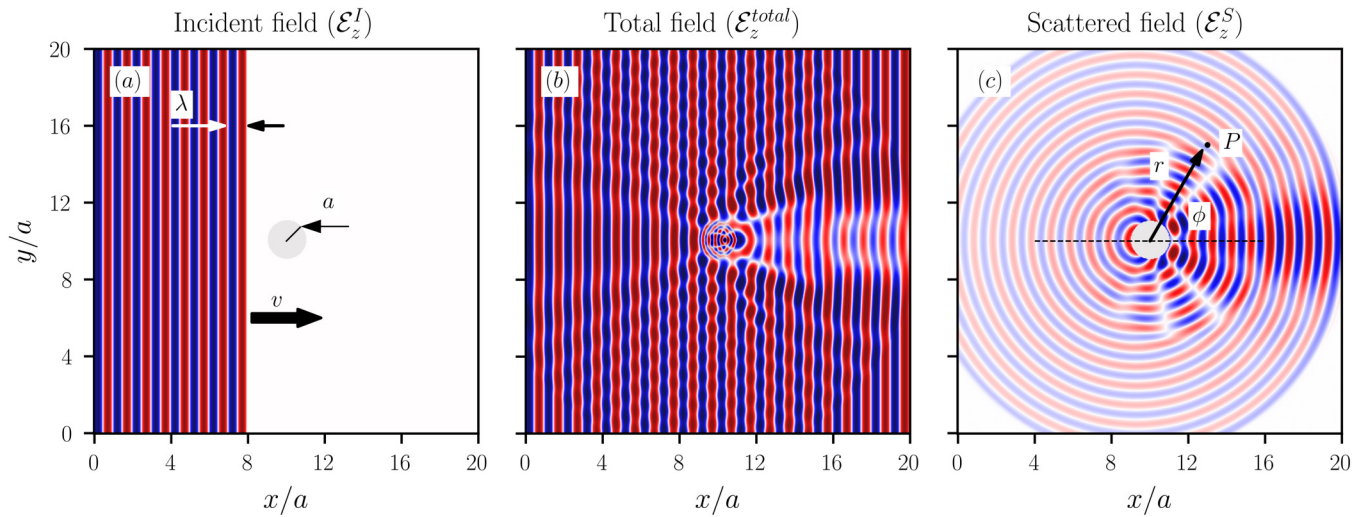
FIG. 1. The simulations involve a square computational domain in the *xy* plane with a circular cylinder of radius *a* placed at the center of the domain. Panel (a) shows the electric field of the incident wave (prior to scattering) of wavelength λ moving along the $+x$ direction. Panel (b) shows the total electric field, and panel (c) shows the scattered electric field outside the scatterer. The side length of the square computation domain is 20 times the radius of the cylinder. The red and blue colors represent, respectively, the positive and negative halves of the electric field.

further validated for scattering by complex geometries such as corrugated circular and elliptical cylinders. Finally, in Sec. VII, we discuss the implications and scope of the findings.

The scattering width is defined as $r \rightarrow \infty$.[34] However, due to the finite size of the computational domain, the near-field must be transformed into the far-field using analytical methods.[50] As a result, the accuracy of the far-field values depends on the calculated near-field data. Thus, in this work, we focus on the near-field; therefore, the term "scattering width" should be interpreted as "near-field scattering width."

II. FORMULATION AND METHODOLOGY

A. Problem definition

Figure 1 represents the system under consideration. A circular cylinder of radius *a* and of infinite length is placed at the center of the domain with its axis oriented along the *z* direction. The medium surrounding the cylinder is vacuum characterized by permittivity ε_0 and permeability μ_0. A monochromatic plane incident wave with TM^z polarization and wavelength λ propagates in the $+x$ direction. This incident wave is shown in Fig. 1(a). The incident wave is a sinusoidal wave, with the electric field along the *z* direction and the magnetic field along the *y* direction. In the figure, we depict the electric field, using red to denote the positive half of the electric field and blue to represent the negative half. As the wave interacts with the cylinder, a portion gets reflected back in the surrounding medium, and the rest transmits through the cylinder.[34] Both the reflected and the transmitted (refracted) waves contribute to scattering.[2] The resultant electric field, referred to as the total electric field ($\mathcal{E}_z^{total}$), arises from the superposition of the incident
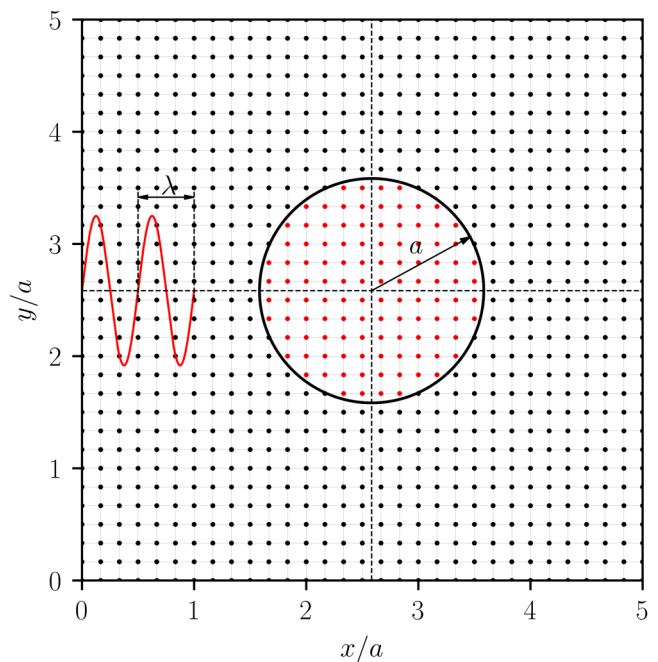

FIG. 2. The schematic illustrates the computational domain for a circular cylinder. The domain is a square with a side length of *L*. The cylinder has a radius of *a*. The incident plane wave of wavelength λ is shown in red. Grid spacing is Δx, equal in the *x* and *y* directions. Red dots mark grids within the scatterer, while black dots represent those outside.

($\mathscr{E}_z^I$) and scattered ($\mathscr{E}_z^S$) electric fields. The total electric field is shown in Fig. 1(b), and the scattered electric field is shown in Fig. 1(c). Point P, marked in Fig. 1(c), is situated at a distance r from the center of the cylinder and at a scattering angle ϕ. The scattering angle refers to the angle between the position vector of point P with the origin set at the center of the cylinder and the direction of propagation of the incident wave. Point P is the location used to calculate the scattered electric and magnetic fields in later sections. The electric fields and magnetic fields in all the figures, including that depicted in Fig. 1, are real numbers in the time domain.

B. Numerical scheme

We propose LBM for solving scattering problems due to its suitability for complex geometries and parallel computing. The fundamental quantity of the LBM is the discrete velocity distribution function, also known as the particle population.[45] The grid is referred to as a lattice, and at each lattice point, the discrete lattice velocity set is represented by a $DdQq$ lattice model. We use the $D3Q7$ lattice model in this work. Here, D represents the space dimension ($=3$), and Q represents the lattice vector set ($=7$).[51] To solve Maxwell's equations, two distribution functions $\mathbf{e}_i(\mathbf{x}, t)$ and $\mathbf{h}_i(\mathbf{x}, t)$ corresponding to the electric and magnetic fields $\mathscr{E}$ and $\mathscr{H}$ are used.[48] The distribution functions $\mathbf{e}_i(\mathbf{x}, t)$ and $\mathbf{h}_i(\mathbf{x}, t)$ are at
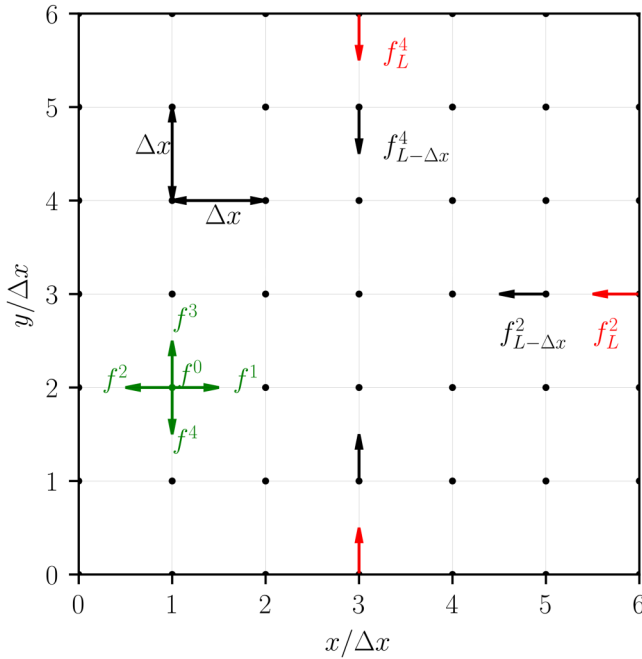

FIG. 3. An illustration of the simulation domain depicting the unknown distribution functions at the boundary in red, accompanied by the corresponding distribution function (distribution function with the same velocity) at the adjacent grid in black. Additionally, five distribution functions are displayed in green to indicate their directions. f^5 and f^6 along the $+z$ and $-z$ directions, respectively, are omitted from this depiction.

TABLE I. Grid resolution and domain size for the calculation of the scattering width on a smooth circular dielectric cylinder of dielectric constant $\varepsilon_r = 2$.

	a/λ					
	0.05	0.1	0.5	1	2	4
$a/\Delta x$	10	10	25	25	200	250
L/a	30	20	15	15	15	15

position $\mathbf{x}$, time t, and have a velocity $\mathbf{c}_i$. Subscript i represents the discrete velocity direction. At each grid point, the macroscopic fields $\varepsilon_r\mathscr{E}$ and $\mu_r\mathscr{H}$ are computed by summing the distribution functions in all the discrete velocity directions,

$$\sum_i \mathbf{e}_i = \varepsilon_r\mathscr{E}, \tag{1a}$$

$$\sum_i \mathbf{h}_i = \mu_r\mathscr{H}. \tag{1b}$$

The lattice Boltzmann equations for the electric and magnetic fields are shown below:

$$\mathbf{e}_i(\mathbf{x} + \mathbf{c}_i\Delta t, t + \Delta t) = \left(1 - \frac{\Delta t}{\tau}\right)\mathbf{e}_i(\mathbf{x}, t) + \frac{\Delta t}{\tau}\mathbf{e}_i^{eq}(\mathbf{x}, t), \tag{2a}$$

$$\mathbf{h}_i(\mathbf{x} + \mathbf{c}_i\Delta t, t + \Delta t) = \left(1 - \frac{\Delta t}{\tau}\right)\mathbf{h}_i(\mathbf{x}, t) + \frac{\Delta t}{\tau}\mathbf{h}_i^{eq}(\mathbf{x}, t). \tag{2b}$$

Here, Δt is the time step. The relaxation time τ equals $1/2$ for Maxwell's equations.[45] The equilibrium distribution functions for the electric and magnetic fields are $\mathbf{e}_i^{eq}$ and $\mathbf{h}_i^{eq}$, respectively. LBM proceeds via successive steps of collision and streaming. The right-hand sides of Eq. (2) are the collision steps, where the distribution functions collide and redistribute themselves at each grid point. The new distribution functions subsequently stream to the neighboring grids[51] as given by the left-hand sides of Eq. (2).

We use the equilibrium distribution function given by Hauser and Verhey,[48]

$$\mathbf{e}_i^{eq} = \begin{cases} \frac{1}{6}(\mathscr{E} - \mathbf{c}_i \times \mathscr{H}) & \text{if } i \neq 0, \\ (\varepsilon_r - 1)\mathscr{E} & \text{if } i = 0, \end{cases} \tag{3a}$$

TABLE II. Grid resolution and domain size for determining the radiation force on a smooth circular PEC cylinder.

	Regime		
	Rayleigh	Mie	GO
$a/\Delta x$	10	25	75
L/a	25	4	3

TABLE III. Grid resolution and domain size for the calculation of scattering width on a smooth circular PEC cylinder.

	a/λ					
	0.05	0.1	0.5	1	2	4
$a/\Delta x$	10	10	25	25	50	100
L/a	30	20	15	15	15	15

$$\mathbf{h}_i^{eq} = \begin{cases} \frac{1}{6}(\mathscr{H} + \mathbf{c}_i \times \mathscr{E}) & \text{if } i \neq 0, \\ (\mu_r - 1)\mathscr{H} & \text{if } i = 0. \end{cases} \quad (3b)$$

Hence, each time step of LBM constitutes (i) computation of the equilibrium distribution functions from the macroscopic fields, (ii) using the equilibrium distribution functions of the previous step to compute new distribution functions in the collision step, and (iii) streaming these new distribution functions to the neighboring grids in the streaming step. In Sec. III, we will discuss the simulation method of the conducting and dielectric cylinders, where we will also discuss the choice of domain, boundary conditions, and initialization.

III. SIMULATION METHOD

Numerical computations are conducted within a square domain, positioning the scatterer at the center. A schematic of the computational domain is depicted in Fig. 2, featuring a circular cylinder. In the figure, the grids inside and outside the scatterer are denoted by red and black dots, respectively. Our simulations encompass all three scattering regimes—Rayleigh, Mie, and geometrical optics—spanning a range of a/λ ratios, from the smallest ratio of 0.02 to the largest of 4.

The LBM described in Sec. II B recovers the two curl equations of Maxwell's equations[45,47,48]

$$\nabla \times \mathscr{E} = -\mu \frac{\partial \mathscr{H}}{\partial t} \quad \text{and} \quad \nabla \times \mathscr{H} = \varepsilon \frac{\partial \mathscr{E}}{\partial t}.$$

We start the simulation with initial condition $\mathscr{E} = \mathbf{0}$ and $\mathscr{H} = \mathbf{0}$ everywhere in the domain. If the initial conditions of the electromagnetic fields satisfy the divergence equations, it will be satisfied at all times.[45,48] Hence, the two divergence equations of Maxwell's equations

$$\nabla \cdot \mathscr{E} = 0 \quad \text{and} \quad \nabla \cdot \mathscr{H} = 0$$

TABLE IV. Grid resolution and domain size for determining the scattering width for a smooth circular dielectric cylinder for $a/\lambda = 0.5$.

	ε_r			
	2	5	10	20
$a/\Delta x$	25	25	25	25
L/a	15	15	15	15

TABLE V. Grid resolution and domain size for the radiation force calculation for smooth circular dielectric cylinder.

		ε_r		
		2	4	5
Rayleigh	$a/\Delta x$	10	10	10
	L/a	15	15	15
Mie	$a/\Delta x$	80	100	150
	L/a	4	4	4
GO	$a/\Delta x$	200	200	240
	L/a	3	3	3

are also satisfied by setting the electric and magnetic fields to zero everywhere in the domain at the first timestep.[48]

Incident wave enters the domain from the left boundary, and we specify the boundary conditions for the electric and magnetic fields. For TM^z polarized plane wave, the boundary conditions at the left boundary of the domain are given by

$$\mathscr{E}_z = \mathscr{E}_0 \sin(\omega t) \quad \text{and} \quad \mathscr{H}_y = -\mathscr{H}_0 \sin(\omega t), \quad (4)$$

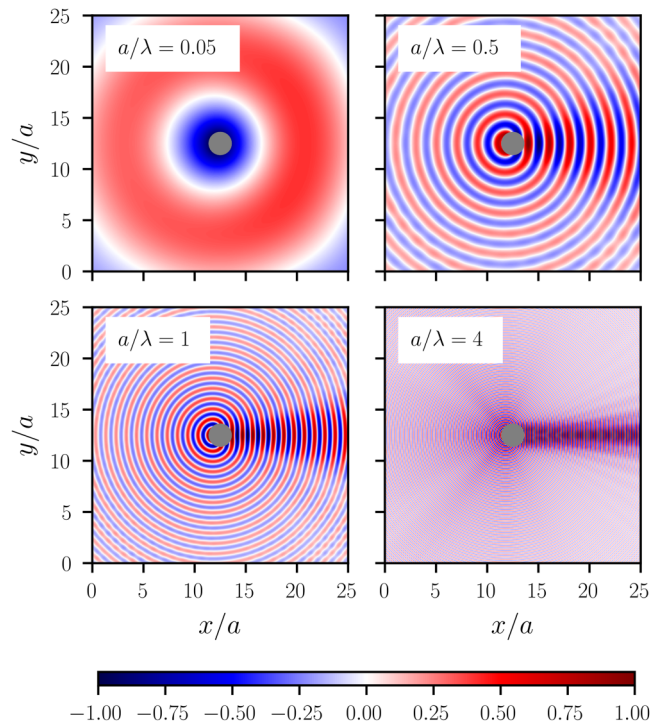while for TE^z polarized plane wave, the boundary conditions at the

FIG. 4. Scattered electric field ($\mathscr{E}_z^S$) from the PEC circular cylinder of radius a for $a/\lambda = 0.05$, 0.5, 1 and 4. Blue represents the electric field's negative half, and red represents the positive half. The colorbar represents the value of the electric field. The circle at the center represents the PEC cylinder.

left boundary of the domain are

$$\mathcal{E}_y = \mathcal{E}_0 \sin(\omega t) \quad \text{and} \quad \mathcal{H}_z = \mathcal{H}_0 \sin(\omega t). \quad (5)$$

As the electric and magnetic fields are known at the grid points of the left boundary from the boundary condition [Eqs. (4) and (5)], we compute the equilibrium distribution functions from the applied fields, and these equilibrium distribution functions stream to the neighboring grid points.

To avoid the reflection from the domain boundaries, we apply the open boundary condition to the remaining three domain boundaries as follows. At the open boundaries, the distribution functions entering the domain are unknown.[40] In the D3Q7 lattice
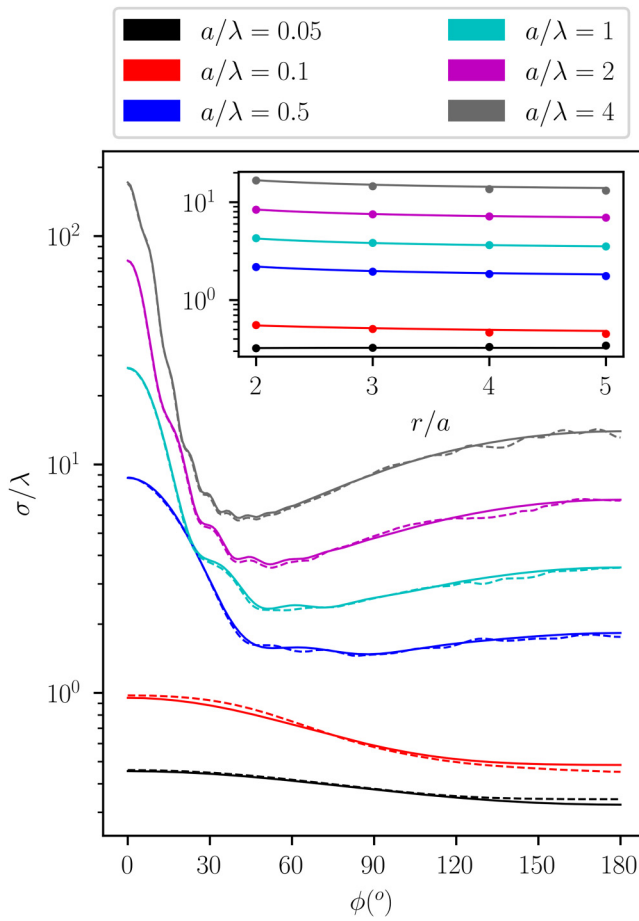

FIG. 5. Scattering widths of the PEC cylinder for different a/λ ratios (covering Rayleigh, Mie, and geometrical optics regimes). The legend is shown at the top of the figure. The outset of the figure shows the bistatic scattering width vs scattering angle ϕ for $r/a = 5$. The solid lines depict the analytical solutions, while the dashed lines represent the results obtained through LBM. The inset shows the monostatic scattering width vs the non-dimensional distance from the center of the cylinder r/a. In the inset, the solid lines represent the analytical solutions, and the markers are from LBM solutions.

model, only one distribution function out of seven is unknown at each grid on the boundary. Thus, we assume that $f_L = f_{L-\Delta x}$, where f_L represents the unknown distribution function at the boundary and $f_{L-\Delta x}$ denotes the corresponding distribution function (distribution function with the same velocity) at the neighboring grid. A schematic representation of the application of open boundary conditions is shown in Fig. 3. The unknown distribution functions are shown in red, and the corresponding known distribution functions at the neighboring grid are shown in black. Additionally, five distribution functions are displayed in green to indicate their directions. f^5 and f^6 along the $+z$ and $-z$ directions, respectively, are omitted from this depiction.

In the following analysis, to calculate the scattered electric and magnetic fields, we solve two problems with the same initial and boundary conditions, one without the scatterer that gives the incident electric and magnetic fields and the other with the scatterer that gives the total electric and magnetic fields. We subtract the incident electric field from the total electric field to get the scattered electric field.

Measures such as the scattering widths at a specific location (r, ϕ) are calculated after the system achieves the steady state, i.e., the amplitude of the electric field does not change with time. In order to determine the average radiation force exerted on the cylinder, it is necessary to obtain the values of the total electric and magnetic fields at the cylinder's surface. To achieve this, we select the closest grid points just outside the cylinder surface. At these grids, we record the total electric and magnetic fields for each time step over one time period. Subsequently, the averages are calculated and utilized them to compute Maxwell's stress tensor at all the identified grids. Finally, we integrate Maxwell's stress tensor over the surface to determine the average radiation force acting upon the cylinder. In Subsections III A and III B, we will discuss the method of simulating the scattering process by the PEC and dielectric cylinders and the parameters used in the simulations.

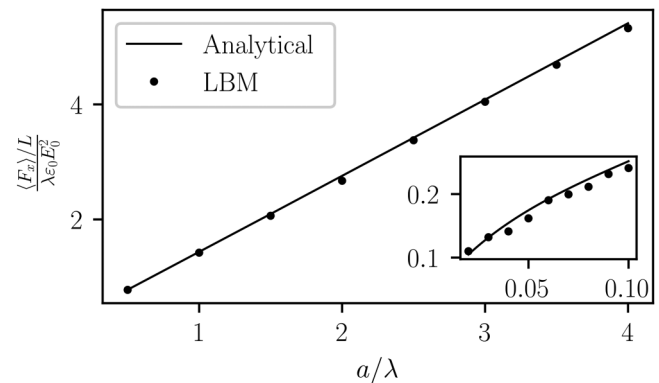**FIG. 6.** Non-dimensional radiation force acting on a PEC cylinder in the x direction plotted as a function of the non-dimensional radius of the cylinder. The main figure shows the force in Mie and geometrical optics regimes, whereas the inset shows the Rayleigh regime. The solid lines represent the analytical solutions, while markers represent the results obtained through LBM.
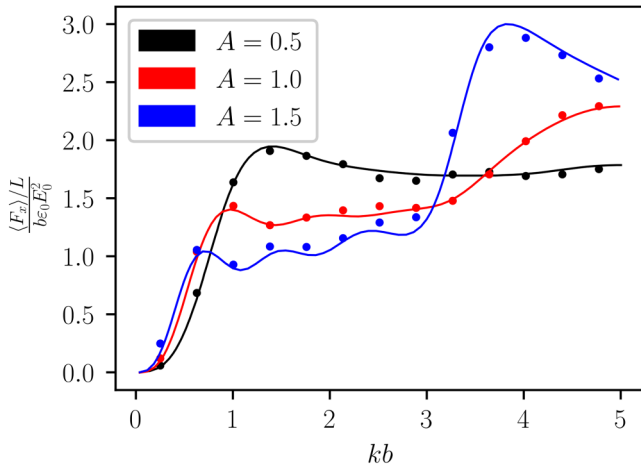
26 November 2024 15:56:32

FIG. 7. Non-dimensional radiation force acting on a corrugated elliptical PEC cylinder in the x direction plotted as a function of the non-dimensional radius of the cylinder. The markers represent the results obtained through LBM, and the continuous lines are the results obtained via the modal expansion method reported by Mitri.[28]

A. PEC cylinder

Given that the electric field inside a PEC material is zero,[52] simulating a PEC cylinder involves setting the electric field to zero inside the cylinder and enforcing relevant boundary conditions at the interface. As the dielectric constant for a PEC approaches infinity, an alternative method to simulate the PEC is by assigning a high value to the dielectric constant. This approach obviates the need to apply any specific boundary condition at the interface. Therefore, we have carried out simulations by selecting $\varepsilon_r = 10\,000$ to model a PEC in this study.

The physics associated with the PEC cylinder varies with the a/λ ratio. As a result, we must adapt our approach by employing different grid resolutions and domain sizes corresponding to distinct a/λ values. Table I outlines the grid resolutions and domain sizes utilized for different a/λ values in the scattering width calculations. Similarly, Table II presents the grid resolutions and domain sizes employed across various regimes to compute the radiation forces acting on the smooth circular PEC cylinders.

The scattered electric field depends on a/λ, r/a, and ϕ.[34] To satisfactorily compare the LBM solutions with the analytical solutions, we need to consider variations in all three parameters, i.e., a/λ, r/a, and ϕ in our simulations. As mentioned earlier, a/λ represents the size parameter of the scatterer, r/a represents the distance from the scatterer, and ϕ represents the angle at which the measurement is taken. We have taken six values of a/λ, i.e., (0.05, 0.1, 0.5, 1, 2, and 4) to cover all three scattering regimes, i.e., Rayleigh, Mie, and geometrical optics regimes. Scattering width is computed at distances ranging from $r/a = 2$ to $r/a = 5$ to examine the effect of choice of measurement location. Similarly, the scattering angles are taken as $\phi = 0^o$ to 180°. Because of the symmetry of the configuration, the scattered electric field and, hence, the scattering width is symmetrical about the x-axis.

B. Dielectric cylinder

The scattered electric field from the dielectric cylinder depends on a/λ, r/a, ϕ, ε_r and μ_r.[34] In this study, we assume that the permittivity of the media inside and outside the cylinder is the same, $\mu_r = 1$. Therefore, unlike the case of PEC cylinders, the

$$H_z^{tot}$$

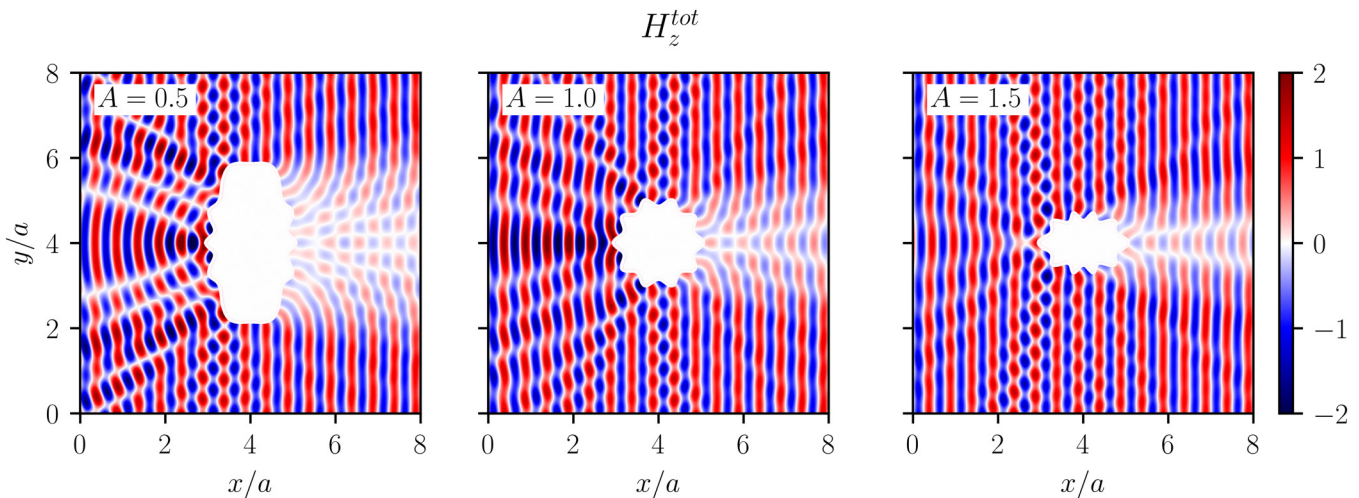**FIG. 8.** A snapshot of the total magnetic field for corrugated elliptical cylinders of different orientations and aspect ratios, controlled by changing the parameter A. All different features, namely, the aspect ratio, the orientation of the object, and the corrugations on the object, affect the scattered field. a is the semi-axis of the ellipse along the horizontal direction.

26 November 2024 15:56:32

TABLE VI. Grid resolution and domain size used for the radiation force calculations on corrugated elliptical PEC cylinders.

		Rayleigh	Mie
$A = 0.5$	$a/\Delta x$	100	200
	L/a	16	8
$A = 1.0$	$a/\Delta x$	100	200
	L/a	8	4
$A = 1.5$	$a/\Delta x$	150	300
	L/a	8	4

physics associated with dielectric cylinders varies not only with a/λ but also with the values of ε_r. Consequently, adjusting the grid resolution and domain size is imperative to capture the scattering process by a dielectric cylinder accurately. Tables III, IV, and V detail the specific grid resolutions and domain sizes utilized in our simulations of dielectric cylinders.

We study two cases: (i) simulations by fixing the dielectric constant $\varepsilon_r = 2$ and varying the other three parameters, i.e., a/λ, r/a, and ϕ, to investigate the dependence on the size of the scatterer on the scattering process, (ii) simulations by fixing the ratio $a/\lambda = 0.5$ and vary r/a, ϕ, and ε_r and analyze the effect of the dielectric constant in the simulations. To comprehensively explore this parametric analysis, we consider three different values of
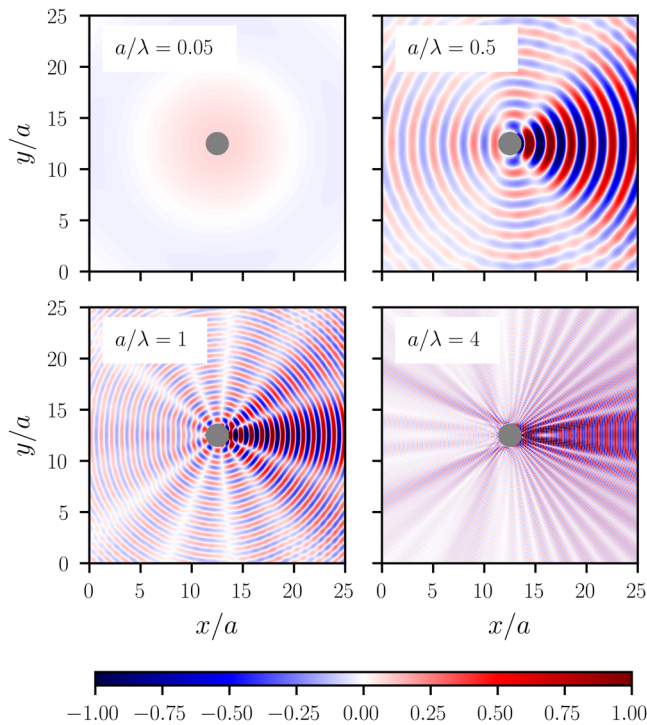

FIG. 9. The same as in Fig. 4, but for the dielectric circular cylinder of dielectric constant $\varepsilon_r = 2$.

$\varepsilon_r = 2, 4$, and 5, alongside a range of a/λ values spanning from 0.02 to 2.6. This selection allows us to cover all three regimes of interest.

IV. RESULTS AND DISCUSSION

A. PEC cylinder

1. Smooth circular cylinder

Figure 4 shows the numerically solved scattered electric field from the PEC cylinder for four different values of a/λ. Here, $a/\lambda = 0.05$ falls under the Rayleigh regime, $a/\lambda = 0.5$ and 1 come under the Mie regime, and $a/\lambda = 4$ comes under the geometrical optics regime. The figure shows that the intensity of the scattered electric field is more uniform around the cylinder for $a/\lambda = 0.05$, that is, the Rayleigh scattering. As a/λ increases, the intensity of the scattered electric field in the forward direction increases, characteristic of Mie scattering and the asymmetry in the intensity further increases in the geometrical optics regime.

Figure 4 illustrated the variation in the intensity of the scattered electric field in various regimes qualitatively, and now we proceed to make a quantitative comparison with the analytical solutions. Figure 5 shows a comparison of the scattering widths for the PEC cylinder for all the three parameters, i.e., (a/λ, r/a and ϕ). The outset of the figure shows the bistatic SW for $r/a = 5$ as a function of scattering angle ϕ for six different a/λ ratios covering all three scattering regimes, as mentioned earlier. The LBM solution of bistatic SW matches the analytical solution well.

The scattering width is not only a function of the scattering angle, but it also depends on the distance r/a at which it is measured. Therefore, in the inset of Fig. 5, we show the comparison of the monostatic SW, i.e., SW for $\phi = 180°$ as a function of r/a for the same a/λ ratios as in case of bistatic SW, the outset of the same figure (Fig. 5). The monostatic SW plot indicates that all LBM solutions agree with the analytical solutions.

Due to the symmetry of the configuration and the fact that the incident wave is a plane wave, the radiation force on the scatterer will act in the direction of the incident wave propagation. Figure 6 compares the solution from LBM and analytical calculations of the radiation force along x direction on the conducting cylinder. Evidently, there is a good match between the two approaches in all three regimes.

In short, the significant match in the SW and the radiation force for the smooth circular PEC cylinder with the predictions of analytical calculations illustrates the versatility of LBM in studying the scattering of PEC objects. In Subsection IV A 2, we will perform a similar study with a corrugated, non-circular PEC cylinder.

2. Corrugated elliptical cylinder

To assess the suitability of LBM for analyzing complex geometries, we now consider the case of corrugated, elliptical cylinders. The results are compared with the solutions reported by Mitri,[28] where a modal expansion method is employed to compute the radiation force per unit length acting on corrugated and smooth elliptical PEC cylinders. In our study, we have reproduced the radiation force calculations for corrugated cylinders using LBM. The surface
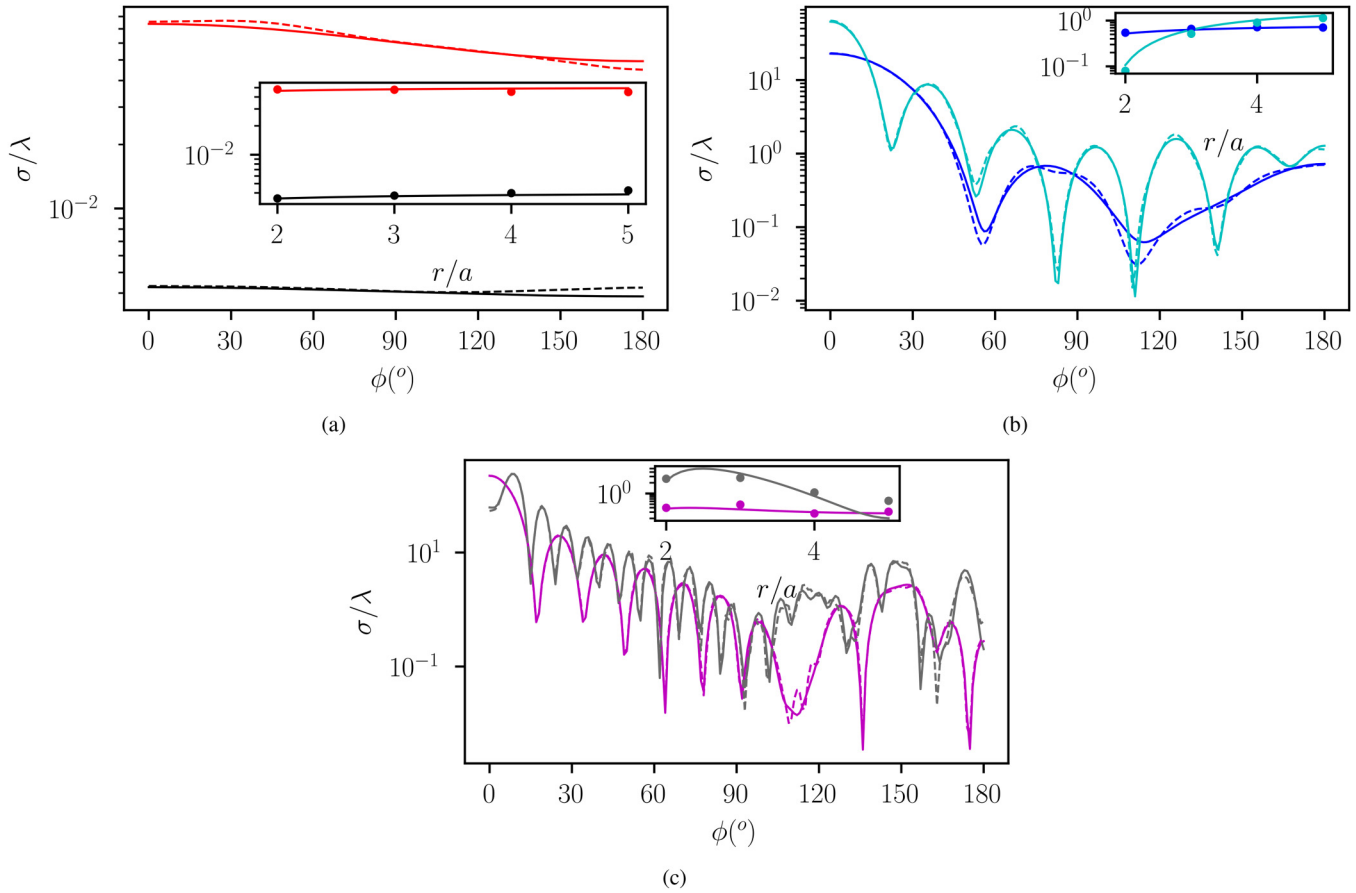
26 November 2024 15:56:32

FIG. 10. Scattering widths of the dielectric cylinder of dielectric constant $\varepsilon_r = 2$ for different a/λ ratios (covering Rayleigh, Mie, and geometrical optics regimes). Panel (a) shows the Rayleigh regime, panel (b) the Mie regime and panel (c) the geometrical optics regime. The legend of Fig. 5 has been used for the color coding. The solid lines depict the analytical solutions, while the dashed lines and markers represent the results obtained through LBM. The outset of the figure shows the bistatic scattering width vs the scattering angle, while the inset shows the monostatic scattering width vs the non-dimensional distance from the center of the cylinder r/a.

of the corrugated cylinder is defined as

$$r = a\left[\frac{1}{\sqrt{(\cos\phi)^2 + (A\sin\phi)^2}} + d\cos(N\phi)\right], \qquad (6)$$

where a represents the semi-axis of the ellipse along the x direction, A denotes the aspect ratio ($A = a/b$), with b being the semi-axis along the y direction, d signifies the depth of corrugation, and N indicates the number of corrugations.

Figure 7 illustrates the radiation force per unit length for corrugated elliptical PEC cylinders under TE^z polarized plane incident wave, considering three different aspect ratios. The comparison between LBM solutions and those obtained through the modal expansion method indicates a good agreement. Additionally, Fig. 8 presents a time snapshot of the z component of the total magnetic field for all three cylinders. Details regarding the grid resolutions

and domain sizes employed for the corrugated elliptical cylinders are summarized in Table VI.

B. Dielectric cylinder

1. Effect of the size of the scattering object

To analyze the effect of the size of the scatterer, we fix the dielectric constant $\varepsilon_r = 2$ of the cylinder and varied the other three parameters, i.e., a/λ, r/a and ϕ. The values of these three parameters are taken to be the same as Sec. IV A.

Figure 9 shows the numerically solved scattered electric field from the dielectric cylinder for various values of a/λ covering three scattering regimes. The values of a/λ are chosen to be the same set reported for the PEC cylinder in Fig. 4. The figure shows that the scattered electric field is more uniform around the cylinder for $a/\lambda = 0.05$, the case of Rayleigh scattering. As a/λ increases, the forward scattering increases, characteristic of Mie scattering and geometrical optics scattering. It is also evident from the figure that the
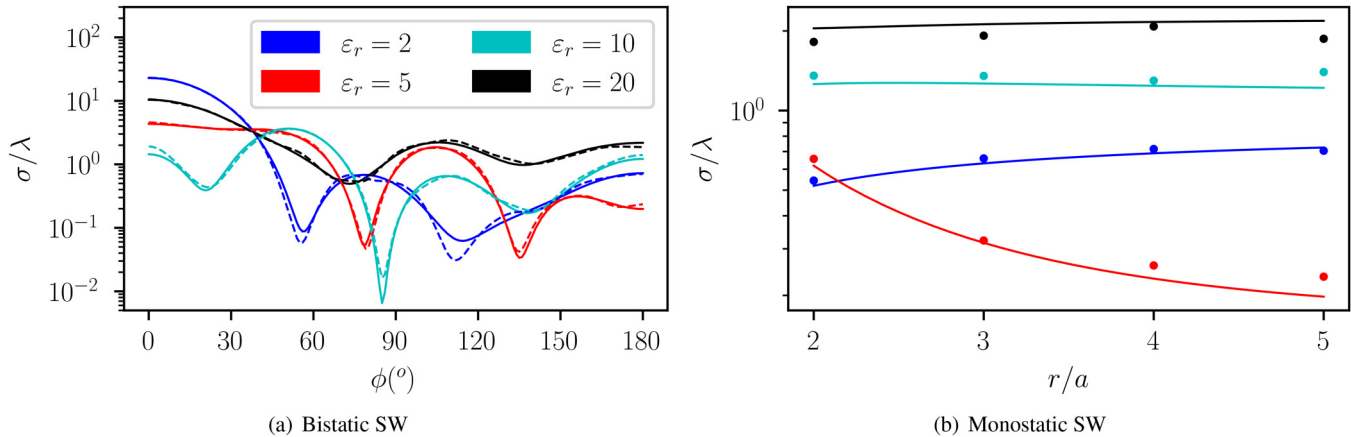
(a) Bistatic SW

(b) Monostatic SW

FIG. 11. Scattering widths of the dielectric cylinders of dielectric constants $\varepsilon_r = 2$, 5, 10, and 20 for $a/\lambda = 0.5$. Panel (a) shows the bistatic scattering width vs scattering angle ϕ for $r/a = 5$, and panel (b) shows monostatic scattering width vs non-dimensional distance from the center of the cylinder r/a. According to the legend, color coding is the same for panels (a) and (b). The solid lines represent the analytical solutions, while the dashed lines and the marker represent LBM solutions.

scattered electric field is weaker as compared to the cases of PEC cylinder reported in Fig. 4. Further, we can see from Fig. 9 that sharp gradients develop in the scattered electric fields at certain angular locations, as indicated by the radial diffused lines, particularly for $a/\lambda = 0.5$, 1, and 4. More of these lines of sharp gradients appear with an increase in the value of a/λ and is a characteristic of the Mie scattering and the geometrical optics scattering.

Now, to compare the solution of LBM with analytical calculations quantitatively, we plotted the scattering widths (SWs) in Fig. 10. For clarity, we have shown the SWs in three sub-figures, each for a different scattering regime, i.e., Rayleigh, Mie, and geometrical optics regimes. The outset and inset of the sub-figures show the bistatic and monostatic scattering widths of the dielectric cylinder, respectively. Figure 10 shows that the solutions determined via LBM are in good agreement with the analytical solutions. The small discrepancy observed in the location of valleys in Figs. 10(b) and 10(c) are due to the high spatial gradient in the electric field. These high spatial gradients in the electric field can also be seen in Fig. 9. Therefore, just like any other numerical method, an increase in the grid resolution can improve the LBM solution if required.

2. Effect of the dielectric constant of the scattering object

In this section, we fix the size of the cylinder by selecting the ratio $a/\lambda = 0.5$ and vary the cylinder's dielectric constant ε_r, measuring distance r/a and scattering angle ϕ. Simulations are done for four values of dielectric constant, i.e., $\varepsilon_r = 2$, 5, 10, and 20. The values of the other two parameters, i.e., r/a and ϕ, are chosen as in the case of the smooth circular PEC cylinder and dielectric cylinder discussed previously.

Figure 11 shows the scattering width (SW) of the dielectric cylinders for $a/\lambda = 0.5$ and dielectric constants $\varepsilon_r = 2$, 5, 10, and 20. The bistatic SW with respect to ϕ for $r/a = 5$ is also shown in Fig. 11(a). Figure 11(b) represents the monostatic SW with respect

to r/a. From the figure, we can see that the LBM solutions (dashed lines) match well with the predictions from the analytical solutions (solid lines).

3. Radiation force on the dielectric cylinder

Figure 12 presents a comparison between the analytical and LBM solutions of the radiation force acting on a dielectric circular cylinder, illustrated as a function of the cylinder's non-dimensional radius a/λ. This comparison encompasses three different values of dielectric constants: $\varepsilon_r = 2$, 4, and 5. Notably, the radiation force on a smooth circular dielectric cylinder exhibits distinct characteristics compared to that on a smooth circular PEC cylinder. It showcases multiple resonance peaks, as depicted in Fig. 12(d). To enhance clarity, we narrow our focus to small ranges of a/λ within each regime—Rayleigh, Mie, and geometrical optics—and depict them in Figs. 12(a)–12(c) respectively. These figures show a significant agreement between the LBM solutions and the analytical solutions. Minor deviations between the two solutions are observed at sharp peaks (resonance peaks). For instance, in Fig. 12(c), for $\varepsilon_r = 4$, we observe two sharp peaks at $a/\lambda = 2.453$ and $a/\lambda = 2.542$. These peaks demonstrate remarkable sensitivity of measurements to changes in a/λ, resulting in notable fluctuations. Even a mere 0.004% and 0.002% alteration in a/λ triggers substantial changes in the value of the radiation force of 40% and 47%, respectively.

We have observed that the method is effective when both the scatterer's geometry and the wavelength are adequately resolved. It is important to focus on the scatterer with the highest dielectric constant in the problem and to resolve the wavelength accordingly. Apart from computation time, we have not encountered any significant limitations. For instance, higher values of a/λ and ε_r require finer grid resolutions, which increase computation time—a common requirement for most numerical methods.
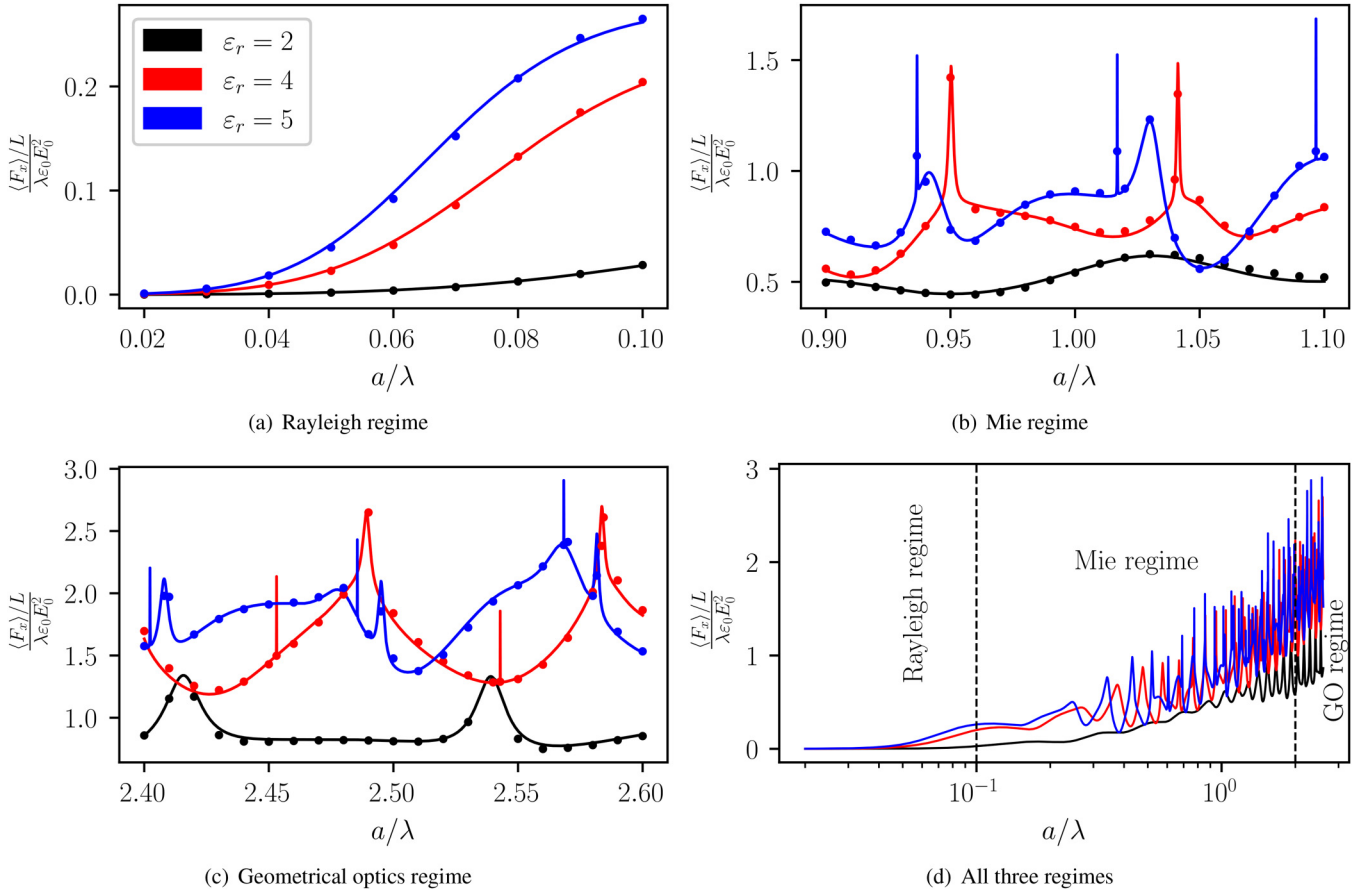
26 November 2024 15:56:32

FIG. 12. Non-dimensional radiation force on a dielectric cylinder of dielectric constant $\varepsilon_r = 2, 4, 5$ along x direction vs non-dimensional radius of the cylinder in (a) Rayleigh, (b) Mie, and (c) geometrical optics regimes. The solid lines depict the analytical solutions, while markers represent the results obtained through LBM. Panel (d) illustrates the solutions from all three regimes plotted together.

In Table VII, we present the percentage error (computed using the exact solutions) in the radiation force for a PEC circular cylinder at various values of a/λ ranging from 0.02 to 20. The table shows that the error remains within 5%. For each simulation, we

ensured that $a/\Delta x \geq 5$ and $\lambda/\Delta x \geq 10$. This indicates that if the geometry and wavelength are properly resolved, we can conduct simulations across a wide range of a/λ values.

In Table VIII, we present the percentage error in the radiation force of dielectric circular cylinders with varying dielectric constants. We ensured that the wavelength within the scatterer is resolved with at least 10 grid points, and the table shows that the error is close to 5%. Notably, the values of a/λ included in this table do not align with resonance peaks, where the physics changes significantly,

TABLE VII. Percentage error in radiation force of PEC circular cylinder for different a/λ values.

a/λ	$a/\Delta x$	$\lambda/\Delta x$	Time (s)	% Error
0.02	5	250	7.20	1.14
0.5	5	10	0.16	3.70
1	10	10	0.22	4.13
2	20	10	0.56	3.10
5	50	10	1.95	2.89
10	100	10	13.20	2.50
20	200	10	103.62	2.45

TABLE VIII. Percentage error in radiation force of dielectric circular cylinders.

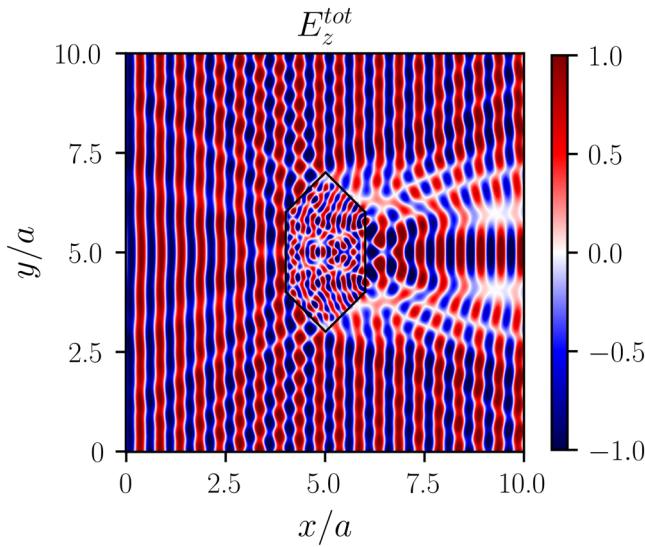| a/λ	ε_r	$a/\Delta x$	$\lambda/\Delta x$ (within scatterer)	Time (s)	% Error
1.0	2	15	10	0.98	4.33
1.0	4	20	10	2.53	3.20
0.9	9	30	11	10.41	5.19

26 November 2024 15:56:32

FIG. 13. Snapshot of the total electric field for a hexagonal dielectric cylinder of dielectric constant $\varepsilon_r = 4$ and $a/\lambda = 2$, where $2a$ is the width of the hexagon along x direction.

FIG. 15. The non-dimensional energy within the computational domain for various grid resolutions is plotted as a function of time for the hexagonal scatterer shown in Fig. 13. The energy is calculated as a moving average over one time period.

necessitating higher grid resolutions at those points. For instance, to accurately capture the resonance peaks at $a/\lambda = 0.95$ and 1.04 in Fig. 12(b), we required a grid resolution of $a/\Delta x = 100$. In contrast, for the non-peak value of $a/\lambda = 1$, a grid resolution of only $a/\Delta x = 20$ was sufficient, as indicated in Table VIII.

We have also included the computation times in seconds in Tables VII and VIII. These calculations were performed utilizing the sequential code. The code was compiled using GCC version 11.4.0 and executed on a computer equipped with an Intel i7-7700 CPU, featuring 4 cores and 32 GiB of RAM.
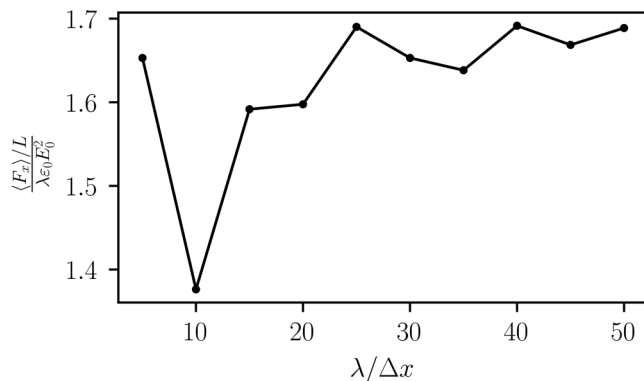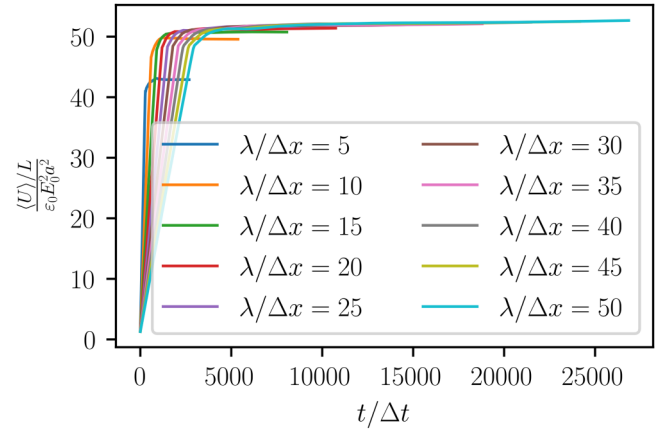
V. SCATTERING BY A SHARP-EDGE CYLINDER

We consider a hexagonal scatterer with a dielectric constant of $\varepsilon_r = 4$ and calculate the total electric field for a TM^z polarized plane wave incident on it, as shown in Fig. 13. To verify the accuracy of the results for this configuration, we calculate the radiation force on the scatterer and the total energy within the computational domain across various grid resolutions ($\lambda/\Delta x = 5 - 50$). The results are presented in Figs. 14 and 15 for the radiation force and energy, respectively. Figure 14 indicates that the radiation force approaches a constant value as the grid resolution increases. Similarly, Fig. 15 shows that the non-dimensional energy remains consistent across all grid resolutions, except for $\lambda/\Delta x = 5$. These observations lead us to conclude that the solutions are stable and accurate, even for scatterers with sharp edges.

For Fig. 13, with the dielectric constant of the scatterer set to $\varepsilon_r = 4$ and a square computational domain with a side length of $L = 500\Delta x$, the computation times are presented in Table IX for both sequential and parallel codes. We utilized OpenMP for parallelization. In the sequential implementation, we combined the collision and streaming processes into a single step to optimize memory usage.[51] The code was executed on the same computer mentioned previously.

FIG. 14. Non-dimensional radiation force as a function of grid resolution for the hexagonal scatterer with a dielectric constant of ($\varepsilon_r = 4$) shown in Fig. 13.

TABLE IX. Computation time for the total electric field of the hexagonal scatterer shown in Fig. 13.

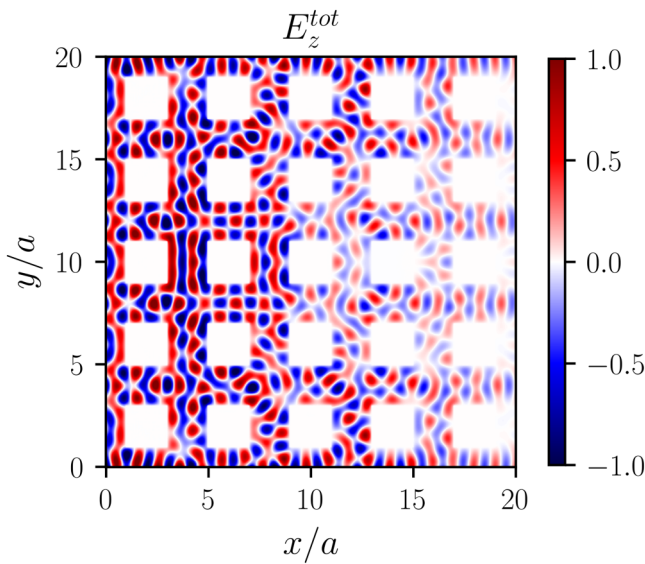| Code	Number of threads	Time (min)
Sequential	…	1.42
Parallel	1	1.67
Parallel	2	0.90
Parallel	3	0.71
Parallel	4	0.63

E_z^{tot}

FIG. 16. A snapshot of the total electric field for an array of PEC square scatterers, each with a side length of $2a$ and $a/\lambda = 1$, where λ denotes the wavelength of the incident wave entering from the left boundary of the domain.

VI. SCATTERING BY MULTIPLE CYLINDERS

To assess the applicability of the LBM for multiple scatterers, we generated an array of uniformly spaced square cylinders made of PEC and dielectric materials. The total electric fields are
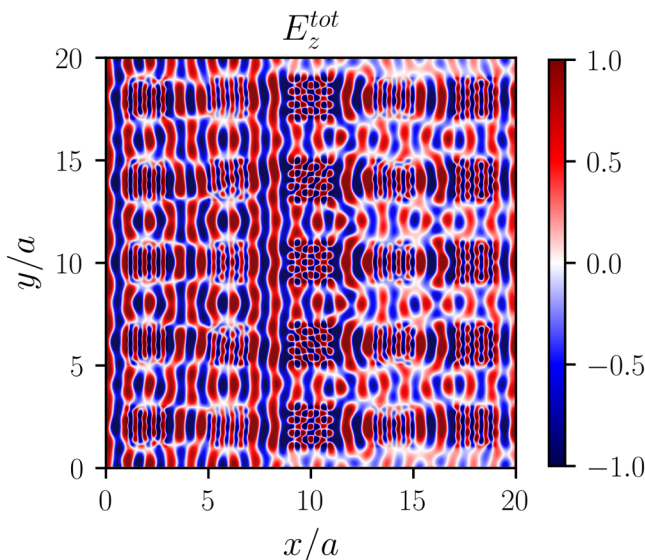
E_z^{tot}

FIG. 17. Same as in Fig. 16 but for dielectric square cylinders of dielectric constant $\varepsilon_r = 5$.
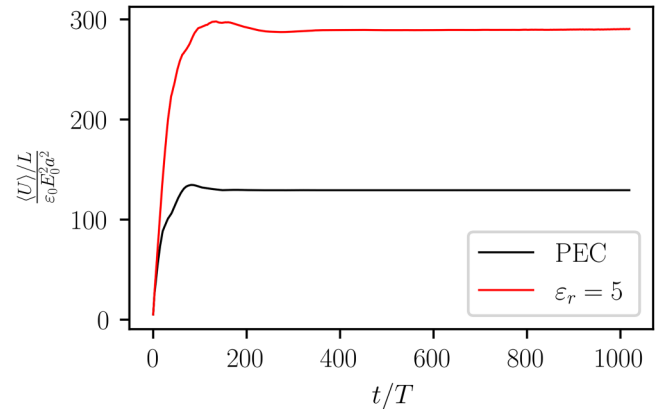

FIG. 18. The non-dimensional energy within the computational domain for the cases illustrated in Figs. 16 and 17 are calculated as a moving average over one time period and plotted against time.

presented in Figs. 16 and 17. The incident wave is a TM^z polarized plane wave with a wavelength λ, entering the computational domain from the left boundary. Each square scatterer has sides measuring 2λ, and the computational domain is a square with a side length of 20λ. The two simulations are identical except for the dielectric constant of the scatterers. In Fig. 16, we set the dielectric constant to $\varepsilon_r = 10\,000$, representing a PEC material, while Fig. 17 features a dielectric constant of $\varepsilon_r = 5$.

To verify the physical validity of the results for the described array of scatterers, we calculated the energy of the entire computational domain for the arrangements shown in Figs. 16 and 17 plotting the results against time in Fig. 18. The simulation was performed over approximately 120 000 time steps, and the figure demonstrates that the energy within the computational domain remains constant.

VII. CONCLUSIONS

In this work, we have validated the lattice Boltzmann method for determining the scattering of and the corresponding radiation force for circular, elliptical, and corrugated cylinders of infinite length. Both PEC and dielectric cylinders are considered. Further, the calculated scattering widths and radiation forces are compared with the analytical solutions. To check the versatility of the method, all relevant parameters for the PEC and dielectric cylinders have been varied, namely a/λ ratio to cover all the scattering regimes, i.e., Rayleigh, Mie, and geometrical optics regimes, scattering angle ϕ, distance r/a from the cylinder and dielectric constant ε_r (for the dielectric cylinder). In all cases, the scattering width and radiation force are calculated. We found an excellent match between numerical results and analytical solutions for all the cases considered. In the case of the radiation force on a corrugated elliptical PEC cylinder, a comparison of LBM results is made with the results obtained using the modal expansion method. We also found a satisfactory agreement between the two methods.

26 November 2024 15:56:32

In instances where minor discrepancies arose in the calculation of scattering width, it was found that such discrepancies were located at points of high spatial gradients in the field. These discrepancies could be mitigated by refining the grid as usual in any numerical method. As for minor discrepancies in the radiation force calculations, they predominantly occur at resonance peaks. These peaks are highly sensitive to variations in the a/λ value, making them challenging to accurately capture. Needless to say, the radiation force at less steep peaks in the radiation force closely matches the analytical solutions. In this work, the computations are conducted assuming pure dielectric materials. However, materials typically exhibit absorption, leading to damping of resonance peaks,[2] a feature that may be incorporated in future studies.

In this work, we confirmed the validity of LBM for both scattering width and radiation force calculations by comparing them with existing analytical and semi-analytical methods, particularly for simple shapes and static scenarios. However, LBM holds potential for dynamic calculations and more complex shapes, whereas traditional analytical and semi-analytical methods may prove less efficient. For instance, Fig. 13 illustrates the scattered electric field for a dielectric hexagonal cylinder, demonstrating the effectiveness of LBM compared to semi-analytical approaches for such geometries. The LBM is capable of handling multiple scatterers, not just a single one. For instance, in Figs. 16 and 17, we illustrate the total electric field generated by an array of PEC square scatterers that are uniformly distributed within the domain. In summary, LBM presents itself as a viable numerical method for both scattering and radiation force calculations.

SUPPLEMENTARY MATERIAL

In the supplementary material, we create an open-source LBM solver for electromagnetic wave scattering and radiation force calculations using the same code for all the analyses presented in this paper.

AUTHOR DECLARATIONS

Conflict of Interest

The authors have no conflicts to disclose.

Author Contributions

Mohd. Meraj Khan: Data curation (lead); Formal analysis (lead); Methodology (equal); Validation (lead); Writing – original draft (lead). **Sumesh P. Thampi:** Conceptualization (equal); Investigation (equal); Methodology (equal); Supervision (equal); Writing – review & editing (equal). **Anubhab Roy:** Conceptualization (equal); Investigation (equal); Methodology (equal); Supervision (equal); Writing – review & editing (equal).

DATA AVAILABILITY

The data that support the findings of this study are available within the article. You can access the code in LBM-for-scattering at https://github.com/mohd-meraj-khan, Ref. 53.

APPENDIX A: TRACTION FORCE DISTRIBUTION ON THE SURFACE OF THE SCATTERER

In order to illustrate the requirement of high grid resolution to capture the radiation force exerted on the scatterer accurately, we consider the case of scattering by a smooth circular dielectric cylinder with a dielectric constant $\varepsilon_r = 4$. Simulations are done using LBM corresponding to three different values of $a/\lambda = 0.91, 0.93$, and 0.95. These three different values correspond to a peak, a valley, and an intermediate value in Fig. 12(b). The radiation force $\langle F_{LBM} \rangle$ is computed by integrating the traction force along the circumference of the cylinder. The error in the radiation force calculated, compared to the analytical prediction, $\langle F_{exact} \rangle$ for these three different values of a/λ is depicted as a function of grid resolution $a/\Delta x$ in Fig. 19. At low grid resolutions, the error remains relatively

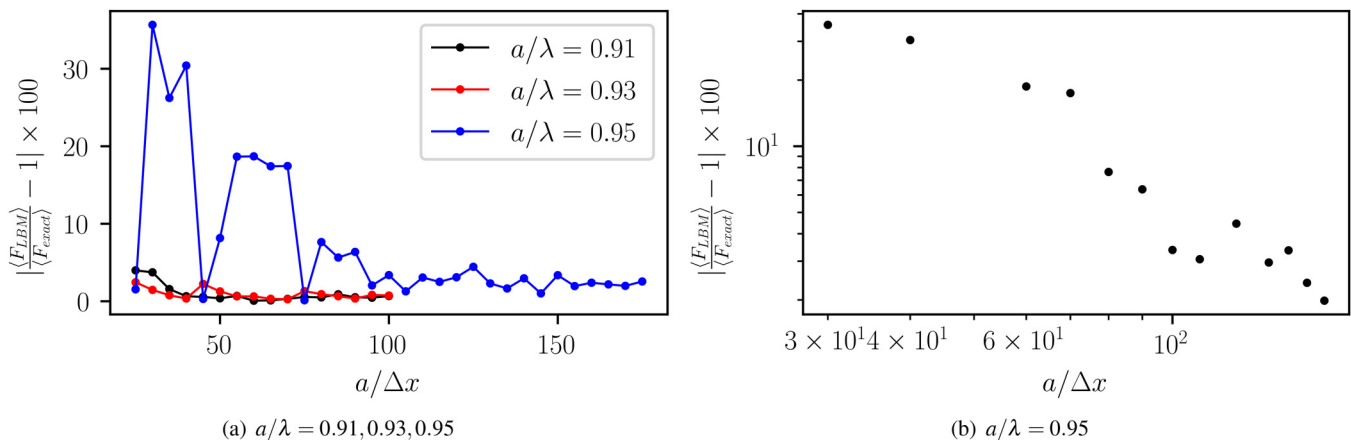(a) $a/\lambda = 0.91, 0.93, 0.95$

(b) $a/\lambda = 0.95$

FIG. 19. Relative error in the average radiation force obtained from LBM calculations $\langle F_{LBM} \rangle$, compared to the analytical prediction, $\langle F_{exact} \rangle$, for a smooth circular dielectric cylinder with dielectric constant $\varepsilon_r = 4$: (a) for three different values of a/λ, corresponding to peak ($a/\lambda = 0.95$) and non-peak values ($a/\lambda = 0.91, 0.93$). (b) Power law decay in error in the calculation of radiation force on increasing the grid resolution for the case of $a/\lambda = 0.95$.
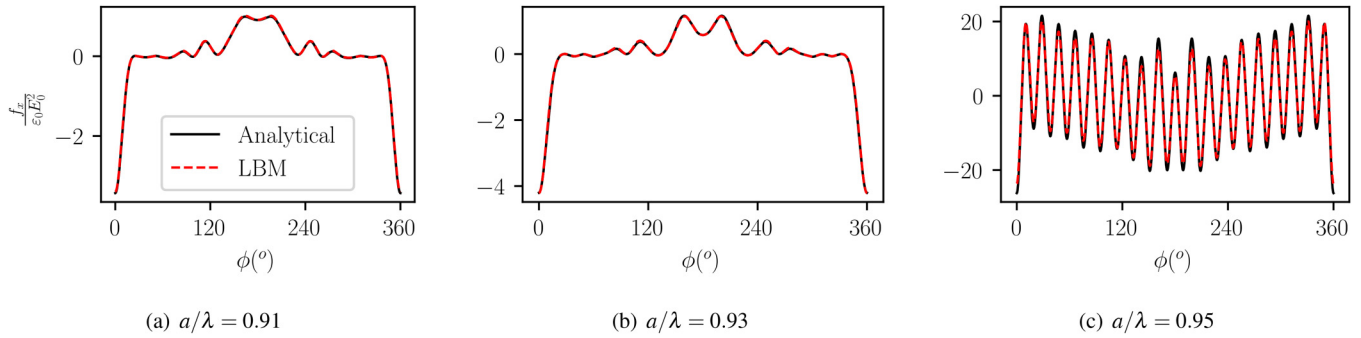
26 November 2024 15:56:32

FIG. 20. Comparison of the instantaneous distribution of traction force on the surface of the scatterer as a function of the azimuthal angle ϕ for the three values of a/λ from LBM simulations and that from the analytical solutions. The solid line represents analytical solutions, while the dashed line represents LBM solutions. The area under the curve, when time-averaged, gives $\langle F_{exact} \rangle$.

low for non-peak values ($a/\lambda = 0.91, 0.93$), but the error is significantly high for the peak value ($a/\lambda = 0.95$).

The requirement of very high grid resolution required for $a/\lambda = 0.95$ can be traced back to the sharp variations in the traction force on the surface of the scatterer when the incident EM wave is scattered. This is illustrated in Figs. 20 and 21 where the traction force obtained from the exact solution and LBM for the three values of a/λ are shown. It is evident from the figure that the traction force for $a/\lambda = 0.95$ (peak) exhibits multiple peaks and valleys. Since the total radiation force is given by the area under the curve, reliable calculation of radiation force corresponding to peak locations such as $a/\lambda = 0.95$ requires high spatial grid resolution in LBM as in any other numerical method. In short, achieving high grid resolution is essential to accurately capture the traction force and, consequently, the radiation force, particularly at peak locations compared to non-peak locations.

In order to further illustrate the capability of LBM to accurately capture the traction force distribution on the surface of the scatterer, we plot a comparison between that obtained from LBM and that from the analytical calculations in Figs. 20 and 21. The instantaneous

traction force distribution is depicted in Fig. 20 for three different a/λ values: 0.91, 0.93, and 0.95, with $a/\lambda = 0.95$ corresponding to a resonance peak. The average traction force calculated over a time period is plotted in Fig. 21. In both figures, the rigid lines are obtained from analytical calculations, and the dashed lines are the results of LBM. In both these figures, we observe that the result from LBM and the analytical solutions overlap for all values of a/λ, illustrating the accuracy of LBM in capturing both instantaneous and average characteristics of the scattering phenomena. As explained previously, small deviations from the analytical predictions can be observed for the case of $a/\lambda = 0.95$ due to the presence of sharp and high-frequency variations in the traction force distribution.

APPENDIX B: TIME VARIATION OF RADIATION FORCE - DETERMINED AS A MOVING AVERAGE

In order to illustrate the capability of LBM in capturing the transient and steady-state behavior and numerical stability, we plot the instantaneous value of the radiation force as a function of time in Fig. 22 for $a/\lambda = 0.91$, 0.93, and 0.95 (peak location). For all
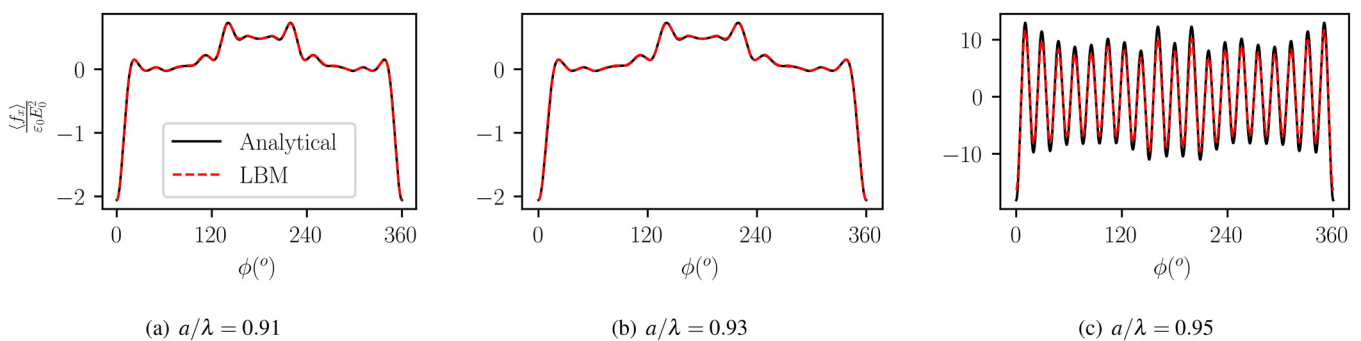

FIG. 21. Comparison of the average value (over a time period) of traction force distribution on the surface of the scatterer as a function of the azimuthal angle ϕ for the three values of a/λ from LBM simulations and that from the analytical solutions. The solid line represents analytical solutions, while the dashed line represents LBM solutions.

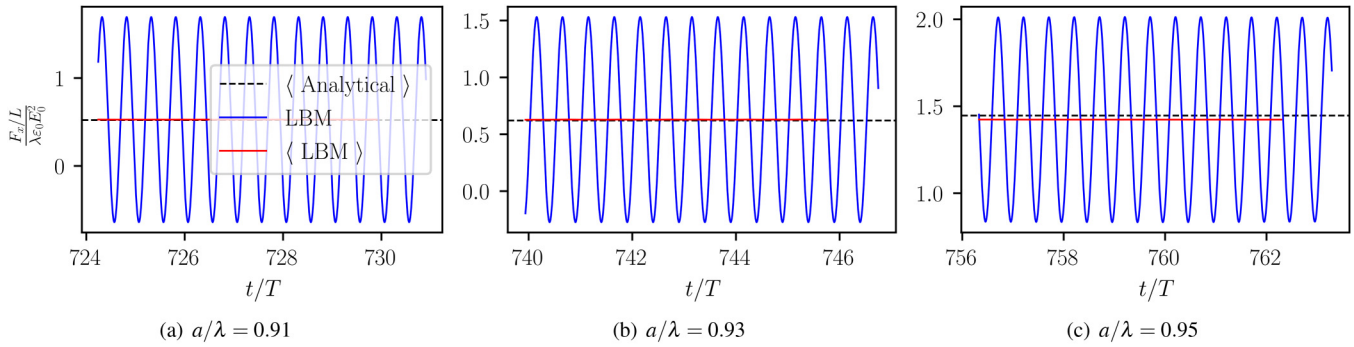(a) $a/\lambda = 0.91$ (b) $a/\lambda = 0.93$ (c) $a/\lambda = 0.95$

FIG. 22. The instantaneous and average radiation force acting on a smooth circular dielectric cylinder with a dielectric constant $\varepsilon_r = 4$ are depicted for three values of $a/\lambda = 0.91, 0.93, 0.95$. The solid blue line represents the instantaneous radiation force computed using LBM. The dashed black line represents the analytically calculated average force, and the solid red line represents the moving average of the force computed using LBM.

three values of a/λ, the instantaneous forces exhibit oscillations with constant amplitude. From the instantaneous values, we determine the average force as a moving average value, which is plotted in the same figure. Further, the radiation force determined from the analytical calculations is plotted for comparison. It may be seen that the moving average values of the radiation force determined from the LBM match with analytical predictions for all three values of $a/\lambda = 0.91, 0.93$ and 0.95. Due to the choice of peak location, $a/\lambda = 0.95$, minor variations can be observed from the analytical solutions, but these variations diminish over time as discussed below (Fig. 23).

Next, we analyze the average radiation force determined as a moving average as shown in Fig. 23. As earlier, three different cases corresponding to $a/\lambda = 0.91, 0.93$ and 0.95 are analyzed. The first two correspond to non-peak locations, and the last one

corresponds to a peak location. Due to high internal reflections at resonance peak,[2] a steady state is achieved after several internal reflections inside the cylinder, as can be seen in the transient state of the force and energy for $a/\lambda = 0.95$ in the figure. Therefore, to calculate the steady-state force at resonance peak, the simulations must be run longer. This is not a limitation of LBM but is a physical phenomenon. Rather, it may be noticed that LBM can capture the transient behavior. The results shown in Fig. 23 correspond to simulations run for nearly 240 000 time steps. Despite the long runs, the numerical method remains stable. In these simulations, the domain size is chosen as $400\Delta x$. Such a large domain ensures that the wave from the left boundary will reach the right boundary in approximately 1200 time steps; however, the simulations run for a much longer time, and we do not observe any sign of spurious reflections from the boundary.
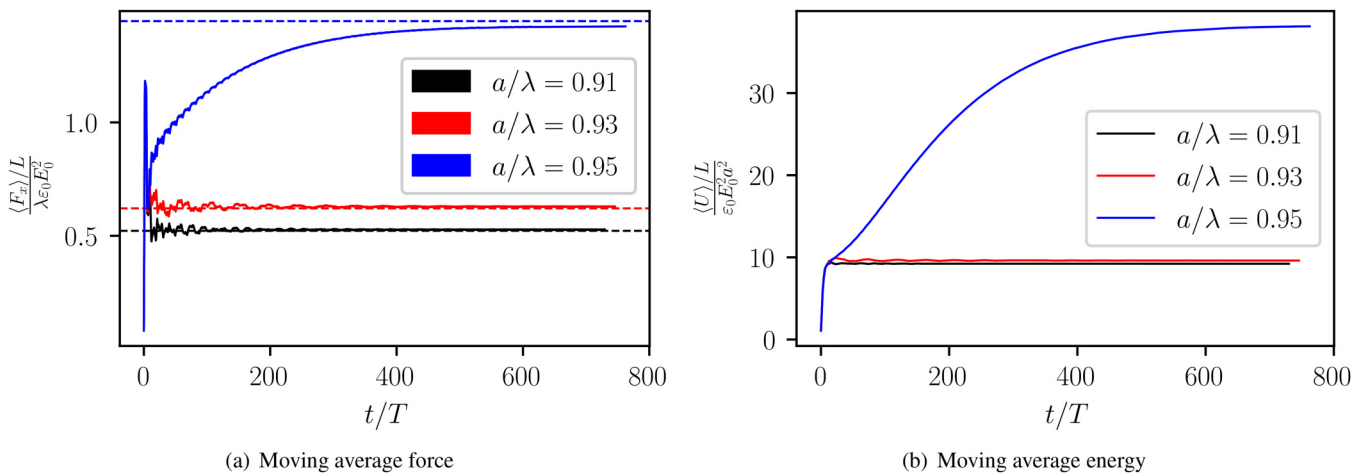

(a) Moving average force (b) Moving average energy

FIG. 23. The moving average value of the (a) radiation force and (b) energy of a smooth circular dielectric cylinder with a dielectric constant $\varepsilon_r = 4$ during the scattering process, plotted as a function of time for three values of a/λ. The dashed lines represent the analytically calculated values of the radiation force, while the solid lines depict the corresponding values obtained using LBM. Here, T is the time period of the incident wave.

REFERENCES

[1] A. V. Osipov and S. A. Tretyakov, *Modern Electromagnetic Scattering Theory with Applications* (John Wiley & Sons, 2017).

[2] H. C. Van de Hulst, *Light Scattering by Small Particles* (Courier Corporation, 1981).

[3] J. A. Stratton, *Electromagnetic Theory* (John Wiley & Sons, 2007).

[4] M. Kerker, *The Scattering of Light and Other Electromagnetic Radiation* (Elsevier, 1969).

[5] C. F. Bohren and D. R. Huffman, *Absorption and Scattering of Light by Small Particles* (John Wiley & Sons, 1998).

[6] J. Li, B. E. Carlson, Y. L. Yung, D. Lv, J. Hansen, J. E. Penner, H. Liao, V. Ramaswamy, R. A. Kahn, P. Zhang *et al.*, "Scattering and absorbing aerosols in the climate system," Nat. Rev. Earth Environ. **3**, 363–379 (2022).

[7] M. T. Falconi and F. S. Marzano, "Weather radar data processing and atmospheric applications: An overview of tools for monitoring clouds and detecting wind shear," IEEE Signal Process. Mag. **36**, 85–97 (2019).

[8] S. Ochoa-Rodriguez, L.-P. Wang, P. Willems, and C. Onof, "A review of radar-rain gauge data merging methods and their potential for urban hydrological applications," Water Resour. Res. **55**, 6356–6391 (2019).

[9] A. Rashidi, S. Domínguez-Medina, J. Yan, D. S. Efremenko, A. A. Vasilyeva, A. Doicu, T. Wriedt, and C. L. Wirth, "Developing scattering morphology resolved total internal reflection microscopy (SMR-TIRM) for orientation detection of colloidal ellipsoids," Langmuir **36**, 13041–13050 (2020).

[10] W. Shao and T. McCollough, "Advances in microwave near-field imaging: Prototypes, systems, and applications," IEEE Microwave Mag. **21**, 94–119 (2020).

[11] M. I. Mishchenko, L. D. Travis, and A. A. Lacis, *Scattering, Absorption, and Emission of Light by Small Particles* (Cambridge University Press, 2002).

[12] A. Ashkin, "Forces of a single-beam gradient laser trap on a dielectric sphere in the ray optics regime," Biophys. J. **61**, 569–582 (1992).

[13] X. Wu, R. Ehehalt, G. Razinskas, T. Feichtner, J. Qin, and B. Hecht, "Light-driven microdrones," Nat. Nanotechnol. **17**, 477–484 (2022).

[14] L.-M. Zhou, Y. Shi, X. Zhu, G. Hu, G. Cao, J. Hu, and C.-W. Qiu, "Recent progress on optical micro/nanomanipulations: Structured forces, structured particles, and synergetic applications," ACS Nano **16**, 13264–13278 (2022).

[15] S. H. Dike and D. King, "The absorption gain and back-scattering cross section of the cylindrical antenna," Proc. IRE **40**, 853–860 (1952).

[16] C.-C. Su, "A surface integral equations method for homogeneous optical fibers and coupled image lines of arbitrary cross sections," IEEE Trans. Microwave Theory Tech. **33**, 1114–1119 (1985).

[17] M. Betterton and M. P. Brenner, "Collapsing bacterial cylinders," Phys. Rev. E **64**, 061904 (2001).

[18] K.-N. Liou and P. Yang, *Light Scattering by Ice Crystals: Fundamentals and Applications* (Cambridge University Press, 2016).

[19] K.-N. Liou, "Light scattering by ice clouds in the visible and infrared: A theoretical study," J. Atmos. Sci. **29**, 524–536 (1972).

[20] L. Rayleigh, "The dispersal of light by a dielectric cylinder," London Edinb. Dublin Philos. Mag. J. Sci. **36**, 365–376 (1918).

[21] J. R. Wait, "Scattering of a plane wave from a circular dielectric cylinder at oblique incidence," Can. J. Phys. **33**, 189–195 (1955).

[22] Q. Cai and K.-N. Liou, "Polarized light scattering by hexagonal ice crystals: Theory," Appl. Opt. **21**, 3569–3580 (1982).

[23] Y. Takano and S. Asano, "Fraunhofer diffraction by ice crystals suspended in the atmosphere," J. Meteorol. Soc. Jpn. Ser. II **61**, 289–300 (1983).

[24] D. De Zutter, "Transverse radiation pressure and torque exerted by a plane electromagnetic wave on a rotating circular cylinder of isotropic material," Appl. Sci. Res. **41**, 17–29 (1984), https://link.springer.com/article/10.1007/BF00418647

[25] J. Xiao and C. T. Chan, "Calculation of the optical force on an infinite cylinder with arbitrary cross section by the boundary element method," JOSA B **25**, 1553–1561 (2008).

[26] C. Rockstuhl and H. P. Herzig, "Rigorous diffraction theory applied to the analysis of the optical force on elliptical nano-and micro-cylinders," J. Opt. A: Pure. Appl. Opt. **6**, 921 (2004).

[27] F. G. Mitri, "Pushing, pulling and electromagnetic radiation force cloaking by a pair of conducting cylindrical particles," J. Quant. Spectrosc. Radiat. Transfer **206**, 142–150 (2018).

[28] F. G. Mitri, "Optical radiation force (per–length) on an electrically conducting elliptical cylinder having a smooth or ribbed surface," OSA Continuum **2**, 298–313 (2019).

[29] F. G. Mitri, "Radiation force and torque on an elliptical cylinder illuminated by a TE-polarized non-paraxial focused Gaussian light sheet with arbitrary incidence," JOSA A **37**, 265–275 (2020).

[30] F. G. Mitri, "Radiation force and torque on perfect electrically–conducting (PEC) corrugated circular and elliptical cylinders in TE or TM polarized plane progressive waves with arbitrary incidence," J. Quant. Spectrosc. Radiat. Transfer **235**, 15–23 (2019).

[31] F. G. Mitri, "Electromagnetic binding and radiation force reversal on a pair of electrically conducting cylinders of arbitrary geometrical cross section with smooth and corrugated surfaces," OSA Continuum **1**, 521–541 (2018).

[32] F. G. Mitri, "Longitudinal and lateral interparticle optical binding and extrinsic radiation force and torque on a pair of lossless dielectric cylinders of arbitrary sizes and the acoustical analogue," Optik **242**, 166831 (2021).

[33] M. I. Mishchenko, "Scale invariance rule in electromagnetic scattering," J. Quant. Spectrosc. Radiat. Transfer **101**, 411–415 (2006).

[34] C. A. Balanis, *Advanced Engineering Electromagnetics* (John Wiley & Sons, 2012).

[35] M. I. Mishchenko, *Electromagnetic Scattering by Particles and Particle Groups: An Introduction* (Cambridge University Press, 2014).

[36] M. Kahnert, "Numerical solutions of the macroscopic Maxwell equations for scattering by non-spherical particles: A tutorial review," J. Quant. Spectrosc. Radiat. Transfer **178**, 22–37 (2016).

[37] J. Kole, M. T. Figge, and H. De Raedt, "Unconditionally stable algorithms to solve the time-dependent Maxwell equations," Phys. Rev. E **64**, 066705 (2001).

[38] F. M. Kahnert, "Numerical methods in electromagnetic scattering theory," J. Quant. Spectrosc. Radiat. Transfer **79**, 775–824 (2003).

[39] S. Chen and G. D. Doolen, "Lattice Boltzmann method for fluid flows," Annu. Rev. Fluid Mech. **30**, 329–364 (1998).

[40] A. Mohamad, *Lattice Boltzmann Method* (Springer, 2011), Vol. 70.

[41] L.-S. Luo and S. S. Girimaji, "Theory of the lattice Boltzmann method: Two-fluid model for binary mixtures," Phys. Rev. E **67**, 036302 (2003).

[42] S. C. Mishra and H. K. Roy, "Solving transient conduction and radiation heat transfer problems using the lattice Boltzmann method and the finite volume method," J. Comput. Phys. **223**, 89–107 (2007).

[43] P. Lallemand and L.-S. Luo, "Theory of the lattice Boltzmann method: Acoustic and thermal properties in two and three dimensions," Phys. Rev. E **68**, 036706 (2003).

[44] P. Dellar, "Electromagnetic waves in lattice Boltzmann magnetohydrodynamics," Europhys. Lett. **90**, 50002 (2010).

[45] M. Mendoza and J. Munoz, "Three-dimensional lattice Boltzmann model for electrodynamics," Phys. Rev. E **82**, 056708 (2010).

[46] S. M. Hanasoge, S. Succi, and S. A. Orszag, "Lattice Boltzmann method for electromagnetic wave propagation," Europhys. Lett. **96**, 14002 (2011).

[47] Y. Liu and G. Yan, "A lattice Boltzmann model for Maxwell's equations," Appl. Math. Modell. **38**, 1710–1728 (2014).

[48] A. Hauser and J. Verhey, "Stable lattice Boltzmann model for Maxwell equations in media," Phys. Rev. E **96**, 063306 (2017).

[49] A. Hauser and J. Verhey, "Comparison of the lattice-Boltzmann model with the finite-difference time-domain method for electrodynamics," Phys. Rev. E **99**, 033301 (2019).

[50] U. S. Inan and R. A. Marshall, *Numerical Electromagnetics: The FDTD Method* (Cambridge University Press, 2011).

[51] T. Krüger, H. Kusumaatmaja, A. Kuzmin, O. Shardt, G. Silva, and E. M. Viggen, *The Lattice Boltzmann Method* (Springer, 2017).

[52] D. J. Griffiths, *Introduction to Electrodynamics* (Pearson, 2013).

[53] LBM-for-scattering. https://github.com/mohd-meraj-khan

26 November 2024 15:56:32